Arabian Journal of Chemistry (2020) 13, 4564–4576

King Saud University

Arabian Journal of Chemistry

www.ksu.edu.sa
www.sciencedirect.com

ORIGINAL ARTICLE

Graphdiyne-actinyl complexes as potential catalytic materials: A DFT perspective from their structural, bonding, electronic and redox properties

Raza ullah shah Bacha [a], Ting-Ting Lin [a], Jun Yao [b], Qing-Jiang Pan [a,*]

[a] *Key Laboratory of Functional Inorganic Material Chemistry (Ministry of Education), School of Chemistry and Materials Science, Heilongjiang University, Harbin 150080, China*
[b] *Inner Mongolia Key Laboratory of Carbon Nanomaterials, College of Chemistry and Chemical Engineering, Inner Mongolia University for Nationalities (IMUN), Tongliao 028000, China*

Received 23 August 2019; accepted 17 October 2019
Available online 31 October 2019

KEYWORDS

Graphdiyne-actinyl;
Electronic structures and bonding;
Redox properties;
Relativistic DFT calculations

Abstract Versatile graphdiyne (GDY) substrate has been modified by numerous transition metals and resulting composites showed excellent photo/electro-catalytic performance. However, GDY materials modified by actinides that are stockpiled waste product due to large-scale use in nuclear industry, are particularly scarce and remains great challenge. To deeply understand the structural properties, GDY complexating actinyl $(An^{m}O_2)^{n+}$ (An = U, Np, Pu; m = VI, V) species with its atomistic pore was investigated by relativistic density functional theory (DFT). The GDY pore was found suitable to hold actinyl species, by forming organometallic An—C dative bonds. This chemical coupling interaction was further confirmed by quantum theory of atoms-in-molecule and electronic structure calculations. The GDY-uranyl(V), for instance, shows a π(U—C) bonding HOMO, which is anticipated to improve electron transfer between ligand and metal. Orbital structures and compositions of complexes suggest their implication towards catalysis, which were further corroborated by calculations on redox potentials of GDY-actinyl complexes. Hence, our results show the potential applications of GDY complexating actinyl species towards novel catalytic surfaces.

1. Introduction

Tremendous efforts have been made in the last decade to discover novel properties and applications of new carbon allotropes, which possess definite advantages of flexibility, light weight and diverse fabrication. (Zhou et al., 2015) Recent advances in two dimensional (2D) carbon materials have revolutionized the modern science. (Cranford et al., 2012) The

* Corresponding author.
E-mail address: panqjitc@163.com (Q.-J. Pan).
Peer review under responsibility of King Saud University.

Production and hosting by Elsevier

https://doi.org/10.1016/j.arabjc.2019.10.005
1878-5352

most widely studied carbon materials these days are carbon nanotubes (CNTs), graphene (GR), graphyne (GY) and graphdiyne (GDY), due to their unique electrical and conductive properties. (Pan et al., 2015; Cranford and Buehler, 2012; Pan et al., 2011)

Graphdiyne (GDY), a 2D carbon material with uniform atomistic pores and rich acetylenic linkages with robust reduction ability, has been used in numerous fields, such as catalysis (Xue et al., 2018; Wang et al., 2017), storage batteries (Yang et al., 2018), and solar cells (Li et al., 2018a, 2018b), due to its intriguing properties such as excellent semiconducting abilities, (Zheng et al., 2012) superior electrical and thermal conductivity and mechanical stability. (Tang et al., 2013; Xiao et al., 2018; Long et al., 2011; Ge et al., 2018) In GDY, the adjacent benzene rings are linked through butadiyne (—C≡C—C≡C—) linkages. (Klappenberger et al., 2015; Haley Michael, 2008) Moreover, in addition to sp^2 hybridized benzene rings, the sp hybridization makes the random angle of rotation of π/π^* perpendicular to the axis, which sorts its possibility to coordinate towards atoms/molecules (Xue et al., 2018). GDY has been an ideal substrate for its direct usage (without prior modifications) in single atom catalysis (SAC) or single nanoparticle catalysis (SNPC), providing better opportunities to fabricate stable catalysts (Chen et al., 2017; Cao et al., 2014; Gao et al., 2018; Lin, 2015). Metal atoms, such as Pt, Pd, Ni, Rh, Ru, Fe, Sc, Ti, Li, Na, K and Ca, and metal oxides like TiO_2 and ZnO have already been used to chemically modify GDY, which maximize their potential industrial usage (Yang et al., 2018; Lin, 2015, 2016; Zi, 2018; Su et al., 2015; Huang et al., 2018; Yin et al., 2018; Tian et al., 2017; Lin et al., 2014; Yang et al., 2013). In this flourishing area, actinide-involving materials, for instance stable high-valent actinyl species $(An^mO_2)^{n+}$ (An=U, Np and Pu; m = VI and V), have been a matter of interest to construct certain intriguing GDY-actinyl-*type* complexes, as these actinyl species have been numerously used for coordination with organic compounds to explore their awaiting catalytic activities. (Su et al., 2015; Liu et al., 2017)

The f-block elements are of great interest because of their applications in many fields like nuclear weapons, nuclear power and medicine (Mason, 2014; Akram et al., 2008; Cournoyer et al., 2015). Amongst them, organic uranium complexes have been extensively studied by revealing its chemical transformations, which in turn catalyzed or activated small inert molecules of N_2, CO_2 and H_2O (Fox et al., 2008; Halter et al., 2016, 2017). In aqueous actinide chemistry, its neptunium and plutonium analogues also have shown some special properties such as their existence in several oxidation states and dramatically high radioactivity. (Altmaier et al., 2013; Wang et al., 2012) The presence of actinyl species, especially $(U^{VI}O_2)^{2+}$ in the residual water from nuclear power plants, heavy industries, uranium mining sites and atomic reactors is a serious concern for environment, and their safe disposal remains a great challenge (Schreckenbach and Shamov, 2010; Zhao et al., 2017). This opens grand opportunities for researchers to design new and beneficial strategies for coordination of $(An^{VI}O_2)^{n+}$, produced as by-products of nuclear processing (Fox et al., 2008). Therefore, it is an ideal way to utilize 2D GDY to chemically combine with actinyl species. On one hand, it directly reduces actinide contamination and effectively uses already stockpiled nuclear waste; on the other hand, the formed GDY-actinyl complexes could be applied as potential catalysts, which may open up a new era of actinyl utilization far beyond nuclear industry (Fox et al., 2008; Halter et al., 2016).

Unfortunately, experimental findings about organic-actinyl catalysts are not conclusive enough, because of difficulty in handling of these radioactive species. Theoretical explorations based on accurate methodology, however, provide useful insight into their unexplored properties (Lavrov et al., 2017). In addition, some of the main reasons which limited the use of these f-block species in catalysis are their complex redox reactions and their extremely complicated electronic structures particularly the cases involving their coordination environments (Gardner et al., 2017; Li et al., 2017). Therefore, the selection of a stable ligand is of prime importance, as the ligand not only stabilizes actinyl species but also tunes electronic behavior of complexes and eventually promotes their catalytic properties (Xue et al., 2018; Li et al., 2017). As exceptional alternative to the previously studied transition-metal modified catalysts, we expect that these actinyls might have the same kind of or even better properties inside GDY, by introducing their valence 5f-electrons for coordination (Fox et al., 2008; Vitova et al., 2017). One recent experimental work has explored actinide based graphene composites for O_2 and H_2O_2 reduction (Sofer et al., 2014), but, there is so far nothing in literature about GDY-actinyl materials.

In this work, we investigated the incorporation of $(An^mO_2)^{n+}$ (An=U, Np and Pu; m = VI and V) to GDY using scalar relativistic DFT. We examined bonding interaction between actinyl and GDY. Furthermore, the electronic and redox properties have been thoroughly studied to unravel their possible photo/electro catalytic performance. The strict retention of GDY-$(An^mO_2)^{n+}$ geometry after optimization and the better balance of structure-properties relationship make for its broader applications perspective, and are expected to form the basis of new catalytic processes of actinide modified 2D-carbon materials (Fagan et al., 1981; Bruno et al., 1984; Lin and Marks, 1990).

2. Computational methods

To simulate the 2D GDY substrate, which is an indefinite system, a single molecular unit with a finite size (i.e. the formula of $C_{30}H_{12}$ that contains a size-suitable pore) was used to accommodate $(An^mO_2)^{n+}$ (An=U, Np, Pu; m = VI, V) in all calculations. For convenience, we used the GDY labeling in the text when describing the single unit. The geometries of GDY-$(An^mO_2)^{n+}$ complexes along with free GDY and aquo-actinyl $[An^mO_2(H_2O)_5]^{n+}$ were fully optimized in the gas phase without any symmetry constraints, using Priroda code (Laikov and Ustynyuk, 2005; Pan et al., 2011). The actinide element includes U, Np and Pu in either V or VI oxidation state. An all-electron (AE) scalar relativistic approach is implemented with projecting out spin-orbit based on the full Dirac equation (Zhong et al., 2016). All calculations were carried out with the PBE level of theory and coupled with double-ζ all-electron basis set (Perdew et al., 1996). Associated frequency calculations were performed at optimized structures. No imaginary values confirm their minimum nature on the potential energy surface. Moreover, thermodynamic data in the gas phase and Infrared (IR) data were obtained simultaneously. Mulliken atomic charges, electron-spin density and

bond orders were calculated on the basis of PBE level of theory Mayer (2003).

One can note that complexes GDY-$(Np^{V}O_2)^+$, GDY-$(Pu^{V}O_2)^+$ and GDY-$(Pu^{VI}O_2)^{2+}$ have more than one electron-spin states (ESS). So we optimized all possible isomers. As seen in Table S1, the highest ESS of each complex is the most stable one. So we will center on the highest ESS in the current work. Additionally, we endeavored to seek the transition state to form GDY-actinyl complex. Although massive efforts were made, unfortunately we did not attain their transition states (Hall et al., 1999; Suwannakham et al., 2018).

The Priroda code have been successfully applied to calculate large complexes at the DFT level, by using the resolution-of-identity (RI) approximation (Pan et al., 2011). Therefore it has a great advantage to be used for calculations involving large organo-actinide molecules, which is the GDY-$(An^{m}O_2)^{n+}$ (m = VI, V) in our case of study (Yao et al., 2014; Schreckenbach et al., 1998). The reliability of the Priroda code was compared and confirmed with the ADF code for relativistic methods (Schreckenbach and Shamov, 2010; Pan et al., 2011; Schreckenbach et al., 1998).

Herein, single point calculations were carried out using Amsterdam density functional (ADF 2014 version) (Ogini et al., 2009; Velde et al., 2001) on the basis of already optimized geometries from Priroda. The re-optimization is avoided in ADF because the geometries and associated properties of complexes do not change substantially (Pan et al., 2011). The convergence criterion of 10^{-6} au was used with an integration parameter of 6.0 in all ADF calculations. The ZORA relativistic method (Lenthe et al., 1999) including spin-orbit coupling (SOC) effects implemented in ADF were used, associated with PBE functional and TZP basis sets. The COSMO model was used to simulate environmental media, in which THF solvent has dielectric constant of 7.6. Therefore, the solvation/SOC energies, atomic charges (Mulliken, Hirshfeld, Voronoi and MDC) as well as electronic structures in solution have been obtained (Velde et al., 2001).

3. Results and discussion

3.1. Structural properties

3.1.1. Optimized geometries parameters

Initially $(An^{m}O_2)^{n+}$ species were centered inside GDY the pore. Optimizations of GDY-$(An^{m}O_2)^{n+}$ complexes show approximately linear actinyl unit and planar GDY. And actinyl takes the central position in the GDY's atomistic pore and is perpendicular to the GDY equatorial plane as shown in Fig. 1. This is reflected by calculated angles of O═An═O close to 180° and O═An─C to 90° (Table 1). The calculated bond lengths of An─C in GDY-$(An^{m}O_2)^{n+}$ ranges from 2.810 to 2.882 Å. These relatively long distances may be caused by relative large size and rigidity of the GDY pore. Consequently, the interaction between central metal atom and acetylenic carbons would be weak. More evidences will be shown below. Recently, transition metals like Fe and Ni have been experimentally electrodeposited onto GDY, and resulting composite materials showed excellent catalytic performance on water splitting (Xue et al., 2018). Extended X-ray absorption fine structure (EXAFS) spectra indicated Fe/Ni─C bond lengths of about 1.5–1.6 Å, where the metal are positioned at the corner of GDY pore. The central position acquired by actinides herein is due to their large size as compared to Fe and Ni ones.

The C1≡C2 distance (a supposed sp-sp triple bond) in the free GDY was calculated to be 1.229 Å, which lengthens in resulting complexes. In ***hexa***-valent ones, the C1≡C2 is 1.238 Å for both U and Np, and 1.237 Å for Pu, while they are 1.237, 1.235 and 1.234 Å in ***penta***-valent complexes. In some previous works, this kind of theoretical strain of GDY upon complexation was evaluated by its acetylenic bond length change (Lu et al., 2018; Shao et al., 2012; Wu et al., 2016). The average bond length of C─C1 bond, connecting benzene ring to acetylenic linkage is 1.402 and 1.405 Å, respectively, as shown in Table 1. The distance of the C2─C3 bond that links two acetylenic units was calculated to be 1.345 Å in GDY and 1.341 Å in complexes (Huang et al., 2018). The average An═O bond distance in GDY-$(An^{VI}O_2)^{2+}$ complexes is 1.760 Å, while it is 1.781 Å in GDY-$(An^{V}O_2)^+$, which are comparable to experimental values of An═O bonds (Austin et al., 2009; Kovács et al., 2015).

The optimized geometry parameters show that acetylenic bond lengths have changed in the resulting complexes relative to the free GDY (Walsh, 1946). Apparently, it is hard to tell the true nature of bonds only from geometry. A conclusion can be drawn by keeping bond orders, vibrational frequencies and orbitals contributions into consideration (Walsh, 1946). For example, it is suggested that actinide 5f orbitals have a great contribution in defining the geometry of GDY-$(An^{m}O_2)^{n+}$ (Vitova et al., 2017). The HOMO and LUMO discussed later will prove the involvement of 5f-orbitals in bond formation between GDY and $(An^{m}O_2)^{n+}$.

For comparison, water ligated analogues $[An^{m}O_2(H_2O)_5]^{n+}$, were taken into account. It is shown that the equatorial An^{VI}─OH_2 bond has an average distance of 2.47 Å with An^{VI}═O around 1.776 Å, which are close to experimental and calculated ones in literature (Kovács et al., 2015). Upon reduction, both equatorial and axial An─O bonds are lengthening, as cases of GDY-$(An^{m}O_2)^{n+}$ (Hay et al., 2000; Walker et al., 1999).

3.1.2. Bond orders

Bond order analysis involves the computation of overlap population between two atoms (Limas and Manz, 2018). It helps to understand and predict chemical behavior of complexes. The bond orders in GDY-$(An^{m}O_2)^{n+}$ complexes were calculated using Priroda code. These analyses could be explained by methods of Walsh (1946), in which bond orders in various compounds were comprehensively studied in terms of ionization potentials and molecular orbitals contributions. Notably, they introduced the mobile bond orders of atomic linkages (especially for π conjugated bonds) in a compound. In this work, the calculated bond orders of equatorial An─C organometallic bond have very small values, ranging from 0.13 to 0.09 for GDY-$(An^{VI}O_2)^{2+}$ and 0.10–0.06 for GDY-$(An^{V}O_2)^+$ (Table 2). Apparently, they are much less than the characteristic formal value for a single bond. Therefore, a weak bond is assigned to the interaction between actinide and acetylenic carbons. The bond order (also denoting bond strength) decreases in going from U─C to Np─C to Pu─C, regardless of whether the actinide oxidation state is VI or V.

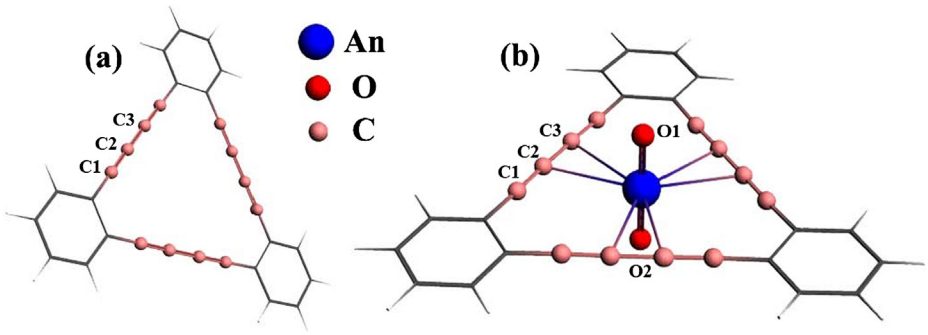

Fig. 1 Optimized structures of (a) Graphdiyne (GDY) and (b) GDY-$(An^{m}O_2)^{n+}$ complexes.

Table 1 Optimized geometry parameters of GDY-$(An^{m}O_2)^{n+}$ complexes. (Bond length in angstrom and angle in degree).

		GDY-$(An^{VI}O_2)^{2+}$			GDY-$(An^{V}O_2)^{+}$		
	GDY	U	Np	Pu	U	Np	Pu
An═O1	–	1.767	1.764	1.755	1.795	1.780	1.768
An═O2	–	1.764	1.762	1.753	1.793	1.781	1.766
An─C	–	2.816	2.831	2.857	2.880	2.880	2.882
C1≡C2[a]	1.229	1.239	1.239	1.239	1.241	1.241	1.241
C2─C3[b]	1.345	1.341	1.341	1.341	1.339	1.342	1.343
C─C1[c]	1.405	1.401	1.400	1.399	1.406	1.405	1.405
O═An═O	–	179.9	179.9	179.1	179.9	179.7	180.0
O─An═C	–	89.7	90.0	89.7	90.0	89.9	90.0
C≡C─An	–	76.2	76.3	78.1	76.5	76.1	76.5

[a] The type of bond (C─C, C═C, C≡C) shown in the table are given as the initial bond orders in GDY-$(An^{m}O_2)^{n+}$ complexes.
[b] Connecting two acetylenic linkages.
[c] Connecting one acetylenic linkage with benzene ring.

Table 2 Bond orders of GDY-$(An^{m}O_2)^{n+}$ complexes.

Bond orders	GDY-$(An^{VI}O_2)^{2+}$			GDY-$(An^{V}O_2)^{+}$			
	U	Np	Pu	U	Np	Pu	GDY
An═O1	2.45	2.43	2.41	2.44	2.42	2.41	–
An═O2	2.44	2.43	2.40	2.42	2.41	2.40	–
An─C	0.13	0.12	0.09	0.10	0.07	0.06	–
C1≡C2[a]	2.13	2.13	2.10	2.17	2.19	2.20	2.25
C2─C3[a]	1.30	1.32	1.35	1.31	1.30	1.30	1.26
C─C1[a]	1.18	1.19	1.19	1.17	1.17	1.17	1.16

[a] See footnotes of Table of 1.

The bond order of acetylenic linkage C1≡C2 from the free GDY ligand was calculated to be 2.25 with a bond distance of 1.23 Å, which is exactly the same as experimentally reported value (Walsh, 1946). In GDY-$(An^{VI}O_2)^{2+}$ (An═U, Np, and Pu) complexes, the calculated C1≡C2 bond orders are 2.13, 2.13 and 2.10 respectively, while they are falling within the range of 2.17–2.20 in GDY-$(An^{V}O_2)^{+}$. These values suggest partially triple bond character for the acetylenic bonds. All the bond orders of C1≡C2 being smaller than the formal value of a triple bond order are resulting from the conjunction effect. On the other hand, smaller bond orders in complexes than in the free GDY is caused by the An─C bonding interaction. In the free GDY, the bond order of C2─C3, in between two acetylenic linkages, was calculated to be 1.16 with 1.40 Å distance, while it is 1.18 (mean value) in GDY-$(An^{m}O_2)^{n+}$ complexes. Additionally, bond orders of C─C1 connecting acetylenic group with phenyl ring do not change significantly after actinide coordination as seen in Table 2, and their values over 1.0 suggest pseudo-double bond character.

The axial An═O bond orders in GDY-$(An^{m}O_2)^{n+}$ have not been disturbed by GDY, which also suggests that GDY ligand has a weak coordination to central actinide atom. We

also note that the calculated An═O bond orders decrease across U, Np and Pu, in consistent with actinide contraction concept.

3.1.3. Vibrational spectra

The structural feature of GDY-$(An^{m}O_2)^{n+}$ (m = VI, n = 2; m = V, n = 1) complexes has further been explained on the basis of vibrational peaks of functional groups. The frequencies were calculated to simulate IR spectra in the range of 0–4000 cm^{-1} as Figs. 2 and S1.

Starting from GDY, calculations (Fig. 2a) show distinct peaks for C─H, C≡C and C═C bonds at 3142, 2213 and 1437 cm^{-1} respectively, which accounts for characteristic peaks of GDY as shown in literatures (Li et al., 2010; Zhang et al., 2016). However, in complexes, for instance in GDY-$(U^{VI}O_2)^{2+}$, corresponding peaks were observed at 3151, 2198 and 1425 cm^{-1}, showing a slight change. It is worth noting that the C≡C stretching vibrational frequency only decreases by 15 cm^{-1} relative to the one of free GDY, suggesting the weak uranyl complexation with the GDY ligand. The red-shift is caused by the flow of electrons, due to the mobile bond nature of acetylene. Similar cases are found in other GDY-actinyl complexes as seen in Figs. 2 and S1.

Apart from GDY-contributed ones, a peak at 880 cm^{-1} was calculated for GDY-$(U^{VI}O_2)^{2+}$ (Fig. 2b), which was assigned to the U═O stretching vibrational mode. The value falls well within the range of experimentally reported IR/Raman data (Gao et al., 2018; Huang et al., 2018; Carter et al., 2018). And Np^{VI}/Pu^{VI}═O stretching vibrational frequencies are found at 848/841 cm^{-1} (exptl, 845/836 cm^{-1}). The actinide-oxo characteristic peaks are close for GDY-$(Np^{VI}O_2)^{2+}$ and GDY-$(Pu^{VI}O_2)^{2+}$, but still show a decreasing trend from U, to Np to Pu. The same manner is observed in GDY-$(An^{V}O_2)^{+}$ series complexes. This general change can be understood by orbitals contributions (discussed below) which show larger-extent of covalent character in GDY-$(U^{m}O_2)^{n+}$ than GDY-$(An^{m}O_2)^{n+}$ (An═Np and Pu).

3.1.4. QTAIM analysis

Chemical bonding in GDY-actinyl complexes has been classified and characterized according to the quantum theory of atoms in molecule (QTAIM) calculations (Bader, 1998, 1991; Lu and Chen, 2013), which focuses on electron density and energy density at bond critical points (BCPs). These parameters have been widely used to determine the strength and explain the nature of chemical bonds in actinide-containing complexes (Pan et al., 2011; Bader, 1991; Mountain and Kaltsoyannis, 2013; Ferraro et al., 2013).

As seen in Tables 3, S2 and S3, calculated QTAIM data at An═O and C≡C BCPs of GDY-$(An^{VI/V}O_2)^{2+/+}$ are large. For example, the ρ values were greater than 0.2, which confirm that the bonds are covalent in nature. The C≡C is a typical covalent bond associated with its negative $\nabla^2\rho$ value, while An═O is assigned to a strongly polarized bond because of having positive $\nabla^2\rho$ values. The ρ values of An═O in GDY-$(An^{VI}O_2)^{2+}$ (An═U, Np and Pu) were computed to be about 0.341, 0.339, 0.331 (mean value), being a little larger than those (0.338, 0.335, 0.329) in GDY-$(An^{V}O_2)^{+}$. This indicates that

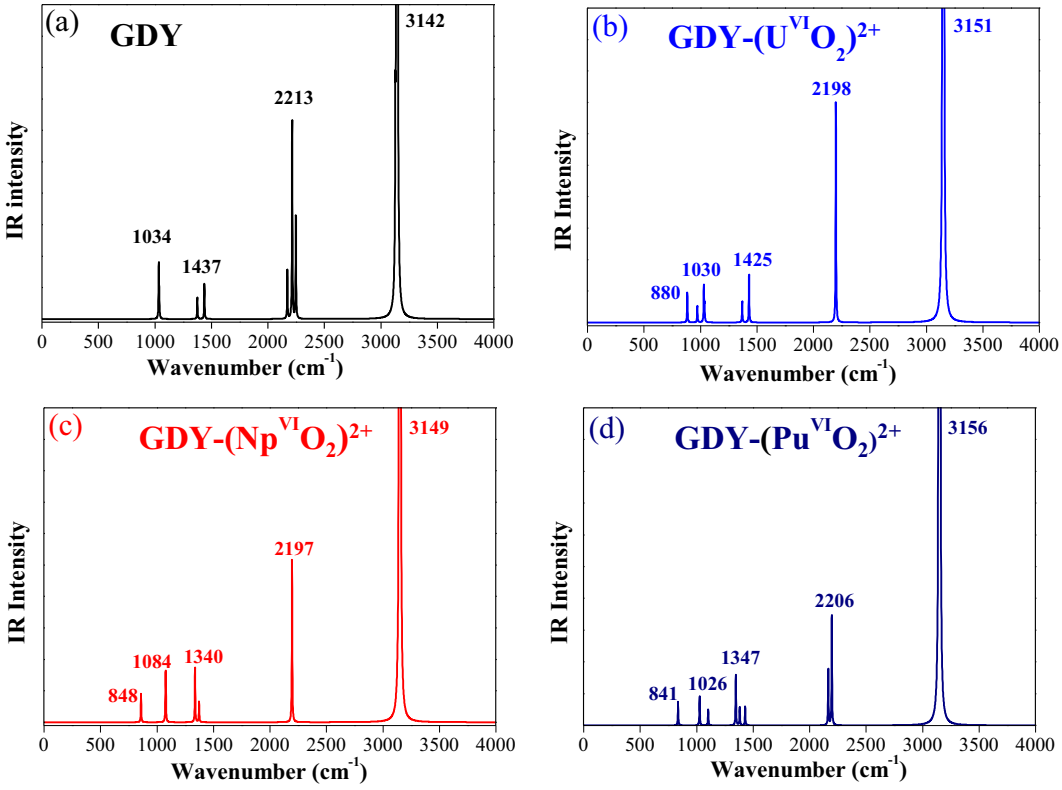

Fig. 2 Theoretically simulated IR spectra of GDY-$(An^{VI}O_2)^{2+}$ complexes.

Table 3 QTAIM analysis showing (ρ), ($\nabla^2\rho$), H(r), V(r), G(r), -G(r)/V(r), ε, and δ in (a.u) and E_{int} in (eV) of GDY-$(U^mO_2)^{n+}$ complexes.[a]

GDY-$(U^{VI}O_2)^{2+}$									
Bonds	ρ(r)	$\nabla^2\rho(r)$	H(r)	V(r)	G(r)	-G(r)/V(r)	ε	δ	E_{int}
An═O1	0.342	0.289	−0.359	−0.790	0.431	0.546	0.000	2.112	−10.753
An═O2	0.341	0.293	−0.358	−0.790	0.432	0.546	0.000	2.122	−10.749
An─C	0.037	0.102	−0.003	−0.032	0.029	0.902	0.498	0.182	−0.430
C1≡C2	0.388	−1.011	−0.513	−0.756	0.243	0.321	0.026	2.211	−10.279
C─C1	0.292	−0.753	−0.286	−0.383	0.097	0.254	0.011	1.198	−5.214
C2─C3	0.316	−0.818	−0.327	−0.450	0.123	0.273	0.036	1.376	−6.124
GDY-$(U^{V}O_2)^{+}$									
Bonds	ρ(r)	$\nabla^2\rho(r)$	H(r)	V(r)	G(r)	-G(r)/V(r)	ε	δ	E_{int}
An═O1	0.339	0.280	−0.355	−0.779	0.425	0.545	0.000	2.035	−10.604
An═O2	0.339	0.283	−0.354	−0.779	0.425	0.545	0.000	2.046	−10.599
An─C	0.034	0.097	−0.002	−0.028	0.026	0.939	0.733	0.156	−0.378
C1≡C2	0.387	−1.011	−0.510	−0.754	0.244	0.324	0.004	2.241	−10.263
C─C1	0.293	−0.751	−0.282	−0.377	0.094	0.251	0.096	1.193	−5.123
C2─C3	0.316	−0.824	−0.328	−0.450	0.122	0.271	0.016	1.379	−6.128

[a] The density and laplacian for C≡C in GDY were 0.382 and −0.100, respectively.

the bond is stronger in ***hexa***-valent complexes than ***penta***-valent counterparts. The QTAIM data for C≡C in complexes do not change significantly compared with those in the free GDY.

Notably, the An─C bonds show small ρ and $\nabla^2\rho$ values, which indicates a dative bond with largely ionic character. The values of An─C bonds (An═U, Np, Pu) are very small (0.037, 0.032, 0.031) in GDY-$(An^{VI}O_2)^{2+}$ and even smaller (0.034, 0.031, 0.030) in GDY-$(An^{V}O_2)^{+}$, which suggests the presence of weak An-C bond. Moreover, the strength of An-C bond is U > Np > Pu, both in VI and V oxidation states. This trend is in agreement with the results of An-C bond orders mentioned above. The -G(r)/V(r) is another parameter for the classification of chemical bonds. For An═O, it is near to 0.5, which is true for its shared interactions, while for C─C -G(r)/V(r) < 0.5, as for their very strong covalent bonding. The -G(r)/V(r) for An─C is 0.5 < -G(r)/V(r) < 1, indicating its partly covalent nature.

3.1.5. Electron spin densities and atomic charges

The atomic charges and electron spin densities were carried out to elaborate the oxidation states and charge carrier mobility of GDY-$(An^mO_2)^{n+}$ complexes. (Fonseca Guerra et al., 2004; Nikolaienko et al., 2016) As seen in Table 4, the calculated actinide charges are 1.492, 1.427 and 1.358 in GDY-$(An^{VI}O_2)^{2+}$ (An═U, Np and Pu) and 1.357, 1.309 and 1.272 in GDY-$(An^{V}O_2)^{+}$, respectively. Larger charges were calculated for An^{VI} than for An^{V}, which follows the simple correlation between atomic charge and oxidation state.

Apparently, the calculated atomic charges for An are much lower from their formal oxidation state in GDY-$(An^mO_2)^{n+}$. However, the electron spin densities may provide good indication for actinide oxidation states in these GDY-actinyl complexes (Yao et al., 2015). The electron spin density of uranium (S_U) in GDY-$(U^{VI}O_2)^{2+}$ is 0.0, as for its close-shell electronic configuration $5f^06d^07s^0$. And, S_U was computed to be 0.86 in GDY-$(U^{V}O_2)^{+}$, which is close to the theoretical formal value of one 5f single electron. Similar results were obtained for GDY-$(An^{V}O_2)^{2+}$ (An═Np and Pu), in that S_{An} was calculated to be 2.09 and 3.30 for, respectively. They are close to the theoretical formal values of 2.0 and 3.0. However, electron spin densities for GDY-$(Np^{VI}O_2)^{2+}$ and GDY-$(Pu^{VI}O_2)^{2+}$ were greatly overestimated, corresponding to 1.61 and 3.03, respectively (Qu et al., 2016). Unfortunately, calculations using ADF code still give similar results (Table S4 and Fig. S2).

Table 4 Atomic charges and electron spin densities of GDY-$(An^mO_2)^{n+}$ complexes.

	GDY-$(An^{VI}O_2)^{2+}$		GDY-$(An^{V}O_2)^{+}$	
	Spin	Charge	Spin	Charge
An═U	0.000	1.492	0.860	1.357
O	0.000	−0.183	−0.030	−0.258
GDY	0.000	−0.134	0.000	−0.119
An═Np	1.606	1.427	2.090	1.309
O	−0.077	−0.194	−0.090	−0.245
GDY	0.000	−0.132	0.000	−0.127
An═Pu	3.027	1.358	3.300	1.272
O	−0.154	−0.193	−0.150	−0.232
GDY	0.011	−0.131	0.000	−0.135

3.2. Electronic properties

Besides their remarkable geometries, GDY-actinyl structures also exhibit encouraging electronic properties, which allows their potential use in photo/electro-catalysis, photoelectric conversion and photoluminescence, similar to the experimentally known GDY-transition metal materials (Pan et al., 2015; Xue et al., 2018; Wang and Chen, 2011). Herein, a systematic study of electronic structures was performed on GDY-$(An^{m}O_2)^{n+}$ complexes, while considering relativistic effects, environmental media and electron correlation (Kovács et al., 2015). The arrangement of molecular orbitals (MO) and the contributions of each fragment of complexes are important as they provide useful information about geometries, bonding nature, spectroscopic properties and more importantly possible reactive property, which in turn can be explicitly used in the design of photo/electro-catalysts.

The band gap of 2D pristine GDY was calculated to be 0.44 eV using the LDA functional in a previous study, while it increased to 1.10 eV at GW (many body level) (Luo et al., 2011). For the quasiparticle GDY system, 1.17 eV (experiment) and 1.29 eV (theory) band gaps were obtained, which is close to the band gap of Si (Luo et al., 2011; Hybertsen and Louie, 1986). Interestingly, the band gap of 2D GDY can be modified by doping acetylenic linkages, extending sp-hybridized carbons to 2D hydrocarbons or placing single metal and metal oxide in the GDY vacancies. It has been shown previously that the direct band gap varies from 0.47 to 2.65 eV by the hydrogenation of sp-hybridized carbons (Zhang et al., 2016). Herein, the calculated HOMO-LUMO gap of a single GDY unit is 2.29 eV at the GGA-PBE level, while involving an environmental media. If we used more extended GDY model (i.e. increasing conjugate degree and layer number), the calculated energy gap would be decreasing and approaching experimentally and theoretically reported band gap of 2D GDY materials. This is evidently caused by the conjunction effect and the interaction between layers of real GDY materials although the latter being weaker. The occupied orbitals of GDY are composed of out-of-plane p_z orbitals as well as in-plane doubly-degenerate p_x and p_y ones. And $\pi(p_z)$ and $\pi^*(p_z)$ character contributes to HOMO and LUMO, respectively.

In contrast, the energy gaps between HOMO and LUMO of GDY-actinyl complexes are much lower (around 0.2 eV), because of actinide 5f orbital's insertion as seen in Fig. 3. HOMO of GDY-$(U^{VI}O_2)^{2+}$ is still mainly contributed by π (GDY), containing 88% $C(p_z)$ (Table S5), while LUMO has primary U(5f) character (90%); the higher-lying unoccupied orbitals, L + 1 ~ L + 3, also have uranium composition over 87%; and the π*(GDY) turns L + 4, possessing 91% $C(p_z)$ character. It is found that the separation energy of HOMO of π(GDY) and L + 4 of π*(GDY) in the uranyl complex is 2.32 eV, being almost the same as HOMO-LUMO gap of the free GDY. In Fig. 4, we drew density of states (DOS) and orbital diagrams, which intuitively support our above assignment.

Unlike those of the uranyl (VI) complex, GDY-$(Np^{VI}O_2)^{2+}$ have orbitals (e.g. HOMO, H-1, LUMO and L + 1) which are contributed by both Np(5f) and π(GDY) character (Table S6 and Fig. S3). Moreover, it has one pure Np(5f)-character orbital H-2 (about 94%). Taken together, these electronic structures agree with calculated spin density that is greater than

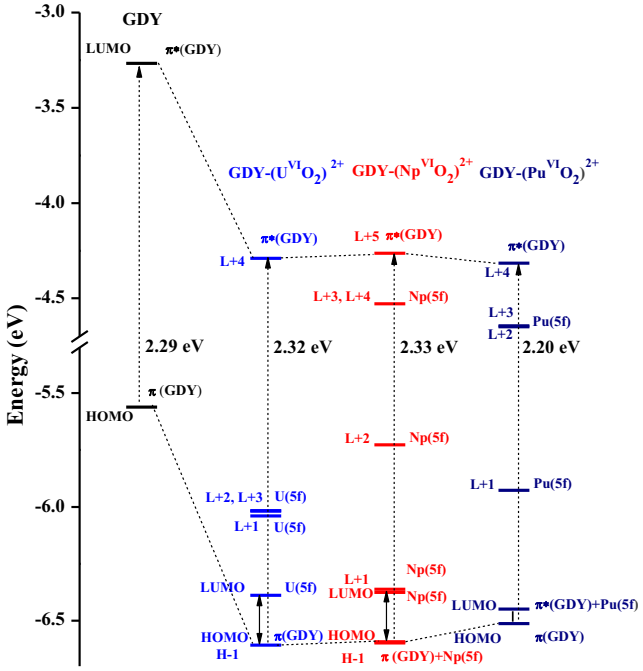

Fig. 3 Energy level diagram of GDY-$(An^{VI}O_2)^{2+}$ and pristine GDY, where orbitals of π(GDY) and π*(GDY) are correlated.

1.0. Similar manners are found in GDY-$(Pu^{VI}O_2)^{2+}$ (Fig. S4 and Table S7), but with one more pure Pu(5f) metal occupied orbital. Similar difference of orbitals between π(GDY) and π*(GDY) is 2.33 and 2.20 eV for Np and Pu complexes, respectively, as seen in Fig. 3.

In case of GDY-$(U^{V}O_2)^{+}$, there is a complete contrast of HOMO composition, which is predominantly (79%) occupied by the U 5f-orbitals, while having less (12%) C p-orbital character (Table S8). Interestingly, they show an overall π bonding interaction, which is visualized in Figs. S5 and S6. The set of lower-energy orbitals (H-1 ~ H-3) have more than 90% π (GDY) character. These reflect the U(V) complex in nature that has only one 5f single electron. The LUMO has even more U(5f) character (86%) and less $C(2p_z)$ contribution (3%). The L + 1 and L + 2 also have greater metal composition. Differently, L + 3 is mainly contributed by π*(GDY). Same cases are observed for GDY-$(Np^{V}O_2)^{+}$ and GDY-$(Pu^{V}O_2)^{+}$, but they show two and three pure metal(5f) filled orbitals, respectively (Tables S9 and S10, as well as Figs. S7, S8, S9 and S10).

The consequences of interaction between actinyl 5f-orbital and acetylenic p-orbital as well as their orbital energies for molecular orbital formation in GDY-actinyl structures prove the mobilization of electrons in the system. The strength of An(5f)-C(p) overlap changes the spin density of actinide inside GDY, leading to intriguing exchange in GDY-$(An^{m}O_2)^{n+}$ complexes (Table 4). We must consider the surface of real GDY materials, which in fact possesses sp-hybridized localized orbitals of strong electronegativity. As shown in Figs. 4, S5 and S6, the electronic structures of uranyl-GDY illustrate stronger overlap of U(5f)-C(p) orbitals from uranium oxidation state VI to V. It is reflected by more U(5f)-C(p) interaction found in HOMO of uranyl(V)-GDY, which shows π(U—C) bonding character. When changing U to Np and Pu that have more 5f electrons in the occupied molecular orbitals, more

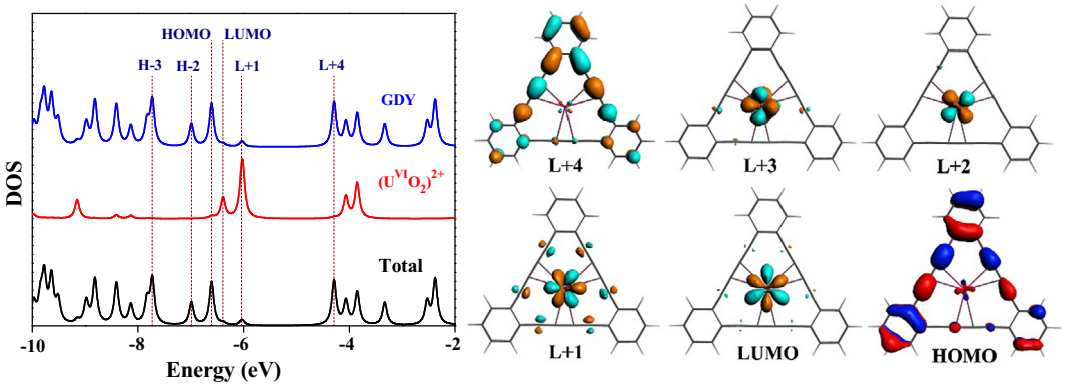

Fig. 4 Density of states (DOS) of α-spin of GDY-$(U^{VI}O_2)^{2+}$ (left) and orbital diagrams with Isosuface value of 0.03 au (right).

orbitals having both An and GDY contributions are present in GDY-$(An^{VI}O_2)^{2+}$. However, one may note that no An-C bonding interaction increases accordingly. The electrons flow in GDY-actinyl complexes may persist for a longer time, because of the reduction ability and the great charge carrier mobility of π-conjugated of sp-sp linkages of GDY (2×10^5 cm^2 V^{-1} s^{-1}) at RT (Xue et al., 2018; Jalili et al., 2015).

Our theoretical study of the electronic behavior of An—C bonds in GDY-$(An^{m}O_2)^{n+}$ complexes are in good agreement with available experimental and theoretical results, which together draws us to the conclusion that the An—C interaction is more covalent than lanthanide-C, but more ionic than transition metal-C (Pepper and Bursten, 1991; Burns and Bursten, 1989).

Organic-metal complexes involving $(An^{m}O_2)^{n+}$, especially those featuring uranium have been used for their applications towards catalysis (Fox et al., 2008; Halter et al., 2017; Pepper and Bursten, 1991). In one of the previously reported UV–Vis spectra of uranyl complexes, intense absorption bands observed were supposed to be due to U—C charge-transfer transitions (Azam et al., 2016). In current work, energy gaps between the high-lying occupied orbitals with π(GDY) character and the low-lying unoccupied orbitals with π*(GDY) were calculated in the range from 2.20 to 2.38 eV for GDY-$(An^{m}O_2)^{n+}$ complexes as marked in Figs. 3 and S11. Comparatively, excitation energies of π(GDY) → 5f and 5f → 5f transitions would be smaller but these transitions often possess extremely small absorptivity. Let's take GDY-$(U^{VI}O_2)^{2+}$ as an example. From a photocatalytic perspective, light radiation on GDY-$(U^{VI}O_2)^{2+}$ complex would lead to π(GDY) → π*(GDY) transition in a large quantum yield. According to their energy gap (2.32 eV, i.e. about 530 nm), the visible light is able to drive the promotion. The photogenerated electrons in π*(GDY) orbitals would easily relax to lower-energy U(5f) virtual orbitals *via* U—C chemical coupling. This accomplishes spatial electron-hole separation. Then these active electrons localized on uranyl part may be applied to catalyze some important and inert small molecules like water, nitrogen gas and CO_2 (Halter et al., 2016, 2017; Evans et al., 2004; Falcone et al., 2018). And thus, GDY-$(U^{VI}O_2)^{2+}$ could be a promising visible-light catalyst. It may work for other GDY-$(An^{m}O_2)^{n+}$ complexes, which also have almost the same HOMO-LUMO gaps as that of GDY-$(An^{VI}O_2)^{2+}$ (Figs. 3 and S11).

3.3. Redox properties

The redox chemistry of actinide complexes is of great importance. The electrochemical process is fundamental and crucial to determine and even predict their reactive properties, prominently those controlling within nuclear fuel cycle. Because of difficulties in handling radioactive actinides and rigid experimental condition for electrochemical measurement, accurate theoretical calculations of redox potentials of actinide-containing complexes, particularly more radiotoxic transuranium species, become appealing, but remains challenging (Arumugam and Becker, 2014; Steele et al., 2013; Yuan et al., 2015)

By giving comprehensive note on the structural and electronic properties, we now proceed towards DFT calculated one-electron redox potentials of GDY-$(An^{m}O_2)^{n+}$. Within GDY, the equatorial coordination of linear actinyl species is satisfied by the inclusion of six explicit organometallic bonds. Accordingly, we predict the role of actinide-GDY bonding in the redox cycle from An(VI) to (V), as well as the electronic transformations related to highest and lowest occupied orbitals, by performing comparative studies with structurally related $[An^{m}O_2(H_2O)_5]^{n+}$ compound. Detailed perceptions into these actinide modified 2D carbon material systems may motivate the design of new catalysts (Halter et al., 2017; Gardner et al., 2017; Denning, 2007).

Generally a free-energy ($\Delta_rG_{ox\text{-}red}$) cycle is considered for calculating redox potentials and such an approach is in good agreement with experimentally known actinide systems (Pan et al., 2011; Hay et al., 2000). In this work, reaction free energy (Δ_rG) of GDY accommodating actinyl species was considered as a measuring parameter. The free energy in the gas phase, G (gas), was obtained from vibrational frequency calculation at 298.15 K, while the COSMO solvation model in the ADF code was used to calculate the solvation free energy G_{sol} of each species in redox reaction (Bao et al., 2016; Klamt and Schüürmann, 1993; Pye and Ziegler, 1999). Moreover, the spin-orbit correction G_{so} was also taken into consideration (Pan et al., 2011; Kovács et al., 2015). And thus in a complete reaction (see below), its Δ_rG(sol) was obtained by the addition of Δ_rG(gas) and Δ_rG_{sol}, and the Δ_rG(sol-so) was gained by adding extra Δ_rG_{so} term.

$$GDY\text{-}(An^{VI}O_2)^{2+} + Fc \rightarrow GDY\text{-}(An^{V}O_2)^{+} + Fc^{+}$$

$$E^0 = \Delta_r G/F$$

where Fc/Fc^+ (ferrocene/ferricenium) is the reference electrode, F is the faraday constant (96485C·mol^{-1}), and E^0 (in V) denotes the reduction potential.

Along with single-electron reaction energies, calculated reduction potentials of actinyl-GDY complexes are presented in Table 5 and plotted in Fig. 5. One can see that E^0(sol), including only solvation energies, monotonously increases from U, Np to Pu complexes. Once spin–orbit coupling (SOC) effects are added, a trend of Np > Pu > U for E^0(sol-so) is observed. Using the same level of theory, E^0(sol-so) of $[An^mO_2(H_2O)_5]^{n+}$ (An=U, Np, Pu) was calculated to show this trend, which well reproduced experimental results (Zhong et al., 2016; Arumugam and Becker, 2014). All together address the importance of SOC effects in accurate calculations of reduction potentials.

E^0(sol-so) of reducing GDY-$(An^mO_2)^{n+}$ (An=U, Np and Pu) from VI oxidation state to V was calculated to be 0.78, 1.05 and 0.88 V, respectively. The last one is comparable to calculated E^0(sol-so) of $[Pu^mO_2(H_2O)_5]^{n+}$ (0.92 V). A smaller E^0(sol-so) was obtained for GDY-$(Np^mO_2)^{n+}$ than for $[Np^mO_2(H_2O)_5]^{n+}$, while GDY-$(U^mO_2)^{n+}$ has much larger E^0(sol-so) than $[U^mO_2(H_2O)_5]^{n+}$. It is worth noting that the larger E^0(sol-so) denotes the easier reduction reaction and the more stable pentavalent complex. For the uranium couple, the coordination of GDY greatly promotes the VI → V reduction reaction with respect to aquo donor. This also originates from GDY-uranyl(V) having greater stabilization than aquo-uranyl(V).

On the basis of above calculated results, we assume that GDY-$(U^mO_2)^{n+}$ (m = VI and V) complexes could be applied for photocatalysis. By comparing with $[U^mO(H_2O)]^{n+}$ species, the coordination with GDY greatly raises the stability of the pentavalent uranyl, which would allow the catalytic cycle from U(VI) to U(V) firstly and then using electron-rich pentavalent complex to reduce some important small molecules like water, CO_2 and N_2 (Halter et al., 2016; Castro-Rodriguez et al., 2003; Schmidt et al., 2012). In recent experimental studies, (U^V)-oxo/imido intermediates have been observed to show the importance in catalytic reactions of small molecules, which opens a new era of U catalysis (Halter et al., 2017; Gardner et al., 2017).

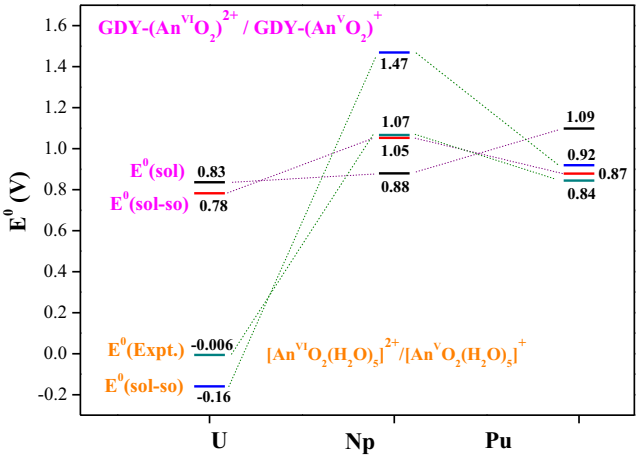

Fig. 5 Plot of calculated redox potentials (E^0 in V) of GDY-$(An^{VI}O_2)^{2+}$/GDY-$(An^VO_2)^+$ couple. In solvation (black bars), solvation with spin orbit coupling (SOC) corrections (red bars), previously calculated solvation/SOC reduction potentials with Fc/Fc^+ reference electrode (blue bars) and experimental reduction potentials against Fc/Fc^+ (gray bars).

4. Conclusions

In this work, a theoretical effort at relativistic DFT level has been made for the construction of GDY-$(An^mO_2)^{n+}$ (An=U, Np and Pu; m = VI and V) complexes. The geometrical structures were used to explain their coordination behavior while electronic structures along with redox properties were used as benchmarks to unleash intriguing catalytic property of actinide modified GDY materials and to deeply understand its relationship with structure.

Table 5 Energies (eV) of single-electron reduction reactions of GDY-actinyl complexes, and reduction potentials E^0 (V) versus the Fc^+/Fc electrode,[a] compared with previously calculated and experimentally determined E^0 for the $[An^{VI}O_2(H_2O)_5]^{2+}/[An^VO_2(H_2O)_5]^+$ couple.

An =		U	Np	Pu
GDY-$(An^{VI}O_2)^{2+}$ + e → GDY-$(An^VO_2)^+$				
Δ_rE(gas)	Calc.	−9.588	−10.016	−9.808
Δ_rG(gas)	Calc.	−9.716	−10.149	−9.736
Δ_rG(sol)	Calc.	−5.978	−6.022	−6.240
Δ_rG(sol-so)	Calc.	−6.004	−6.274	−6.100
GDY-$(An^{VI}O_2)^{2+}$ + Fc → GDY-$(An^VO_2)^+$ + Fc^+				
E^0(sol)[b]	Calc.	0.836	0.880	1.098
E^0(sol-so)[b]	Calc.	0.782	1.053	0.879
$[An^{VI}O_2(H_2O)_5]^{2+}$ + Fc → $[An^VO_2(H_2O)_5]^+$ + Fc^+				
E^0(sol-so)	Calc.[c]	−0.160	1.470	0.920
E^0	Expt.[c]	−0.006	1.067	0.844

[a] The Δ_rG(sol) and Δ_rG(sol-so) of the Fc^+/Fc reference electrode were calculated to be −5.142 and −5.221 eV, respectively, using the ADF code.
[b] E^0 was obtained according to equation in the text.
[c] Calculated and experimental values were taken from Ref. Zhong et al. (2016).

The optimized geometries of GDY-$(An^{m}O_2)^{n+}$ show that approximately linear actinyl species takes the central position in GDY's atomistic pore, in which the An forms organometallic bonds with acetylenic carbons of GDY. This structure differs from experimentally known GDY-Fe/Ni catalysts where the metal is located in the corner of GDY pore. QTAIM analysis and calculated bond orders indicate intrinsic C → An dative bonds. The IR spectra have been calculated to verify characteristic peaks of functional groups in the complexes. Calculated electron-spin densities and atomic charges together get information about oxidation state of actinide in complexes, which are in agreement with orbital structure analysis.

Compared with the one calculated for the free GDY, the incorporation of actinyl greatly narrows HOMO-LUMO energy gaps of GDY-actinyl complexes due to actinide 5f orbitals' insertion. Notably, these complexes possess separation energies between the high-lying occupied orbital with π (GDY) character and the low-lying unoccupied orbital with π*(GDY) close to GDY. The HOMO of GDY-$(U^{V}O_2)^{+}$, for instance, is composed by 79% U(5f) and 12% π(GDY), featuring an overall π bonding interaction between them. GDY-uranyl complexes illustrate increasing U-C overlap from metal valence of VI to V. When changing U to Np and Pu, more orbitals having contributions of both An and GDY are found, GDY-$(An^{VI}O_2)^{2+}$ series complexes for example. However, no An-C bonding interaction increases accordingly.

Reduction potentials of GDY-actinyl complexes have been computed to show the order of Np > Pu > U, being the same trend as experimentally determined and theoretically calculated values of $[An^{m}O_2(H_2O)_5]^{n+}$. Interestingly, a much more positive reduction potential was attained for GDY-uranyl than aquo-uranyl complexes, which demonstrates that GDY is able to stabilize uranium(V) ion to a larger degree.

In brief, associated with experimentally known GDY-Fe/Ni and GR-U/Th catalytic materials, the comprehensive study of bonding, electronic structures and redox properties shows that our GDY-actinyl complexes could be applied as photo/electrocatalysts. Further theoretical study of GDY-actinyl complexes catalyzing small molecules like water and CO_2 is in processing.

Declaration of Competing Interest

We declare that we have no conflict of interest.

Acknowledgment

This work is supported by the Heilongjiang Touyan Innovation Team Program. The National Natural Science Foundation of China (21671060 and 21273063) and the Inner Mongolia Natural Science Foundation-China (2017MS0222) are appreciated. The authors are grateful to Dr. Dimitri Laikov for providing us with the Priroda code.

Appendix A. Supplementary material

Supplementary data to this article can be found online at https://doi.org/10.1016/j.arabjc.2019.10.005.

References

Akram, M., Khattak, N.U., Ullah, I., Tufail, M., 2008. Fission track estimation of uranium concentrations in liquid homeopathic medicine samples. Rad. Meas. 43, S527–S531.

Altmaier, M., Gaona, X., Fanghänel, T., 2013. Recent advances in aqueous actinide chemistry and thermodynamics. Chem. Rev. 113, 901–943.

Arumugam, K., Becker, U., 2014. Computational redox potential predictions: applications to inorganic and organic aqueous complexes, and complexes adsorbed to mineral surfaces. Minerals 4, 345.

Austin, J.P., Sundararajan, M., Vincent, M.A., Hillier, I.H., 2009. The geometric structures, vibrational frequencies and redox properties of the actinyl coordination complexes ($[AnO_2(L)^{n}]^{m}$; An = U, Pu, Np; L = H_2O, Cl^-, CO_3^{2-}, $CH_3CO_2^-$, OH^-) in aqueous solution, studied by density functional theory methods. Dalton Trans. 5902–5909.

Azam, M., Velmurugan, G., Wabaidur, S.M., Trzesowska-Kruszynska, A., Kruszynski, R., Al-Resayes, S.I., Al-Othman, Z.A., Venuvanalingam, P., 2016. Structural elucidation and physicochemical properties of mononuclear Uranyl(VI) complexes incorporating dianionic units. Sci. Rep. 6, 32898.

Bader, R.F.W., 1991. A quantum theory of molecular structure and its applications. Chem. Rev. 91, 893–928.

Bader, R.F.W., 1998. A bond path: a universal indicator of bonded interactions. J. Phys. Chem. A 102, 7314–7323.

Bao, Z., Zhao, H.-B., Qu, N., Schreckenbach, G., Pan, Q.-J., 2016. Theoretical investigation of low-valent uranium and transuranium complexes of a flexible small-cavity macrocycle: structural, formation reaction and redox properties. Dalton Trans. 45, 15970–15982.

Bruno, J.W., Duttera, M.R., Fendrick, C.M., Smith, G.M., Marks, T.J., 1984. New stoichiometric and catalytic organometallic chemistry with actinides. C-H activation and phosphine/phosphite coordination chemistry. Inorgan. Chim. Acta 94 (5), 271–277. https://doi.org/10.1016/S0020-1693(00)87455-1.

Burns, C.J., Bursten, B.E., 1989. Covalency in f-element organometallic complexes: theory and experiment. Comments In. Chem. 9, 61–93.

Cao, X., Zheng, B., Rui, X., Shi, W., Yan, Q., Zhang, H., 2014. Metal oxide-coated three-dimensional graphene prepared by the use of metal-organic frameworks as precursors. Angew. Chem. 126, 1428–1433.

Carter, K.P., Kalaj, M., Kerridge, A., Ridenour, J.A., Cahill, C.L., 2018. How to bend the uranyl cation via crystal engineering. Inorg. Chem. 57, 2714–2723.

Castro-Rodriguez, I., Nakai, H., Gantzel, P., Zakharov, L.N., Rheingold, A.L., Meyer, K., 2003. Evidence for alkane coordination to an electron-rich uranium center. J. Am. Chem. Soc. 125, 15734–15735.

Chen, Z., Molina-Jirón, C., Klyatskaya, S., Klappenberger, F., Ruben, M., 2017. 1D and 2D graphdiynes: recent advances on the synthesis at interfaces and potential nanotechnological applications. Ann. Phys. 529, 1700056.

Cournoyer, M.E., Costigan, S.A., Schake, B.S., 2015. Why is weapons grade plutonium more hazardous to work with than highly enriched uranium?. J. Chem. Health Saf. 22, 2–9.

Cranford, S.W., Brommer, D.B., Buehler, M.J., 2012. Extended graphynes: simple scaling laws for stiffness, strength and fracture. Nanoscale 4, 7797–7809.

Cranford, S.W., Buehler, M.J., 2012. Selective hydrogen purification through graphdiyne under ambient temperature and pressure. Nanoscale 4, 4587–4593.

Denning, R.G., 2007. Electronic structure and bonding in actinyl ions and their analogs. J. Phys. Chem. A 111, 4125–4143.

Evans, W.J., Kozimor, S.A., Ziller, J.W., Kaltsoyannis, N., 2004. Structure, reactivity, and density functional theory analysis of the six-electron reductant, $[(C_5Me_5)_2U]_2(\mu\text{-}\eta^6\text{:}\eta^6\text{-}C_6H_6)$, synthesized via a new mode of $(C_5Me_5)_3M$ reactivity. J. Am. Chem. Soc. 126, 14533–14547.

Fagan, P.J., Manriquez, J.M., Maatta, E.A., Seyam, A.M., Marks, T. J., 1981. Synthesis and properties of bis(pentamethylcyclopentadienyl) actinide hydrocarbyls and hydrides. A new class of highly reactive f-element organometallic compounds. J. Am. Chem. Soc. 103, 6650–6667.

Falcone, M., Barluzzi, L., Andrez, J., Fadaei Tirani, F., Zivkovic, I., Fabrizio, A., Corminboeuf, C., Severin, K., Mazzanti, M., 2018. The role of bridging ligands in dinitrogen reduction and functionalization by uranium multimetallic complexes. Nat. Chem.

Ferraro, F., Páez-Hernández, D., Murillo-López, J.A., Muñoz-Castro, A., Arratia-Pérez, R., 2013. Antenna effect by organometallic chromophores in bimetallic d–f complexes. J. Phys. Chem. A 117, 7847–7854.

Fonseca Guerra, C., Handgraaf, J.-W., Baerends, E.J., Bickelhaupt, F.M., 2004. Voronoi deformation density (VDD) charges: assessment of the Mulliken, Bader, Hirshfeld, Weinhold, and VDD methods for charge analysis. J. Comput. Chem. 25, 189–210.

Fox, A.R., Bart, S.C., Meyer, K., Cummins, C.C., 2008. Towards uranium catalysts. Nature 455, 341.

Gao, Y., Cai, Z., Wu, X., Lv, Z., Wu, P., Cai, C., 2018. Graphdiyne-supported single-atom-sized Fe catalysts for the oxygen reduction reaction: DFT predictions and experimental validations. ACS Catal. 8, 10364–10374.

Gardner, B.M., Kefalidis, C.E., Lu, E., Patel, D., McInnes, E.J.L., Tuna, F., Wooles, A.J., Maron, L., Liddle, S.T., 2017. Evidence for single metal two electron oxidative addition and reductive elimination at uranium. Nat. Commun. 8, 1898.

Ge, C., Chen, J., Tang, S., Du, Y., Tang, N., 2018. Review of the electronic, optical, and magnetic properties of graphdiyne: from theories to experiments. ACS Appl. Mater. Interfaces.

Haley Michael, M., 2008. Synthesis and properties of annulenic subunits of graphyne and graphdiyne nanoarchitectures. Pure Appl. Chem., 519

Hall, M.B., Margl, P., Náray-Szabó, G., Schramm, V.L., Truhlar, D. G., van Santen, R.A., Warshel, A., Whitten, J.L., 1999. Quantum Catalysis: The Modeling of Catalytic Transition States, Transition State Modeling for Catalysis. American Chemical Society, pp. 2–17.

Halter, D.P., Heinemann, F.W., Bachmann, J., Meyer, K., 2016. Uranium-mediated electrocatalytic dihydrogen production from water. Nature 530, 317.

Halter, D.P., Heinemann, F.W., Maron, L., Meyer, K., 2017. The role of uranium–arene bonding in H_2O reduction catalysis. Nature. Chem. 10, 259.

Hay, P.J., Martin, R.L., Schreckenbach, G., 2000. Theoretical studies of the properties and solution chemistry of AnO_2^{2+} and AnO_2^{+} Aquo Complexes for An = U, Np, and Pu. J. Phys. Chem. A 104, 6259–6270.

Huang, C., Li, Y., Wang, N., Xue, Y., Zuo, Z., Liu, H., Li, Y., 2018. Progress in research into 2D graphdiyne-based materials. Chem. Rev.

Huang, C., Li, Y., Wang, N., Xue, Y., Zuo, Z., Liu, H., Li, Y., 2018. Progress in eesearch into 2D graphdiyne-based materials. Chem. Rev. 118, 7744–7803.

Hybertsen, M.S., Louie, S.G., 1986. Electron correlation in semiconductors and insulators: band gaps and quasiparticle energies. Phys. Rev. B 34, 5390–5413.

Jalili, S., Houshmand, F., Schofield, J., 2015. Study of carrier mobility of tubular and planar graphdiyne. App. Phy. A 119, 571–579.

Klamt, A., Schüürmann, G., 1993. COSMO, a new approach to dielectric screening in solvents with explicit expressions for the screening energy and its gradient. J. Chem. Soc., Perkin Trans., 799–805

Klappenberger, F., Zhang, Y.-Q., Björk, J., Klyatskaya, S., Ruben, M., Barth, J.V., 2015. On-surface synthesis of carbon-based scaffolds and nanomaterials using terminal alkynes. Acc. Chem. Res. 48, 2140–2150.

Kovács, A., Konings, R.J.M., Gibson, J.K., Infante, I., Gagliardi, L., 2015. Quantum chemical calculations and experimental investigations of molecular actinide oxides. Chem. Rev. 115, 1725–1759.

Laikov, D.N., Ustynyuk, Y.A., 2005. PRIRODA-04: a quantum-chemical program suite. New possibilities in the study of molecular systems with the application of parallel computing. Russ. Chem. Bul., 54, pp. 820–826.

Lavrov, H.V., Ustynyuk, N.A., Matveev, P.I., Gloriozov, I.P., Zhokhov, S.S., Alyapyshev, M.Y., Tkachenko, L.I., Voronaev, I. G., Babain, V.A., Kalmykov, S.N., Ustynyuk, Y.A., 2017. A novel highly selective ligand for separation of actinides and lanthanides in the nuclear fuel cycle. Experimental verification of the theoretical prediction. Dalton Trans. 46, 10926–10934.

Lenthe, E.v., Ehlers, A., Baerends, E.-J., 1999. Geometry optimizations in the zero order regular approximation for relativistic effects. J. Chem. Phys. 110, 8943–8953.

Li, J., Gao, X., Jiang, X., Li, X.-B., Liu, Z., Zhang, J., Tung, C.-H., Wu, L.-Z., 2017. Graphdiyne: a promising catalyst-support to stabilize cobalt nanoparticles for oxygen evolution. ACS Catal. 7, 5209–5213.

Li, J., Jiu, T., Duan, C., Wang, Y., Zhang, H., Jian, H., Zhao, Y., Wang, N., Huang, C., Li, Y., 2018a. Improved electron transport in MAPbI3 perovskite solar cells based on dual doping graphdiyne. Nano Energy 46, 331–337.

Li, J., Jiu, T., Chen, S., Liu, L., Yao, Q., Bi, F., Zhao, C., Wang, Z., Zhao, M., Zhang, G., Xue, Y., Lu, F., Li, Y., 2018b. Graphdiyne as a host active material for perovskite solar cell application. Nano Lett. 18, 6941–6947.

Li, G., Li, Y., Liu, H., Guo, Y., Li, Y., Zhu, D., 2010. Architecture of graphdiyne nanoscale films. Chem. Commun. 46, 3256–3258.

Limas, N.G., Manz, T.A., 2018. Introducing DDEC6 atomic population analysis: part 4. Efficient parallel computation of net atomic charges, atomic spin moments, bond orders, and more. RSC Adv. 8, 2678–2707.

Lin, Z.-Z., 2015. Graphdiyne as a promising substrate for stabilizing Pt nanoparticle catalyst. Carbon 86, 301–309.

Lin, Z.-Z., 2016. Graphdiyne-supported single-atom Sc and Ti catalysts for high-efficient CO oxidation. Carbon 108, 343–350.

Lin, Z., Marks, T.J., 1990. A kinetic, mechanistic, and molecular mechanics investigation of olefin insertion into organoactinide-hydride bonds. Metal, olefin, ancillary ligand, and diastereoselection effects. J. Am. Chem. Soc. 112, 5515–5525.

Lin, Z.-Z., Wei, Q., Zhu, X., 2014. Modulating the electronic properties of graphdiyne nanoribbons. Carbon 66, 504–510.

Liu, H., Ghatak, T., Eisen, M.S., 2017. Organoactinides in catalytic transformations: scope, mechanisms and Quo Vadis. Chem. Commun. 53, 11278–11297.

Long, M., Tang, L., Wang, D., Li, Y., Shuai, Z., 2011. Electronic structure and carrier mobility in graphdiyne sheet and nanoribbons: theoretical predictions. ACS Nano 5, 2593–2600.

Lu, T., Chen, F., 2013. Bond order analysis based on the Laplacian of electron density in fuzzy overlap space. J. Phys. Chem. A 117, 3100–3108.

Lu, C., Yang, Y., Wang, J., Fu, R., Zhao, X., Zhao, L., Ming, Y., Hu, Y., Lin, H., Tao, X., Li, Y., Chen, W., 2018. High-performance graphdiyne-based electrochemical actuators. Nat. Commun. 9, 752.

Luo, G., Qian, X., Liu, H., Qin, R., Zhou, J., Li, L., Gao, Z., Wang, E., Mei, W.-N., Lu, J., Li, Y., Nagase, S., 2011. Quasiparticle energies and excitonic effects of the two-dimensional carbon allotrope graphdiyne: theory and experiment. Phy. Rev. B 84, 075439.

Mason, C.F., 2014. Uranium and nuclear power: the role of exploration information in framing public policy. Res. Energy Econ. 36, 49–63.
Mayer, I., 2003. Perturbational Methods.
Mountain, A.R.E., Kaltsoyannis, N., 2013. Do QTAIM metrics correlate with the strength of heavy element–ligand bonds?. Dalton Trans. 42, 13477–13486.
Nikolaienko, T.Y., Bulavin, L.A., Hovorun, D.M., 2016. Can we treat ab initio atomic charges and bond orders as conformation-independent electronic structure descriptors?. RSC Adv. 6, 74785–74796.
Ogini, F.O., Elder, P.J.W., Britten, J.F., Vargas-Baca, I., 2009. An investigation of $(C_5H_5)Fe(C_5H_4–C(OBF_3)–CH_3)$. Can. J. Chem. 87, 1055–1062.
Pan, Q.-J., Guo, Y.-R., Li, L., Odoh, S.O., Fu, H.-G., Zhang, H.-X., 2011. Structures, spectroscopic properties and redox potentials of quaterpyridyl Ru(ii) photosensitizer and its derivatives for solar energy cell: a density functional study. Phy. Chem. Chem Phy. 13, 14481–14489.
Pan, Y., Wang, Y., Wang, L., Zhong, H., Quhe, R., Ni, Z., Ye, M., Mei, W.-N., Shi, J., Guo, W., Yang, J., Lu, J., 2015. Graphdiyne–metal contacts and graphdiyne transistors. Nanoscale 7, 2116–2127.
Pan, L.D., Zhang, L.Z., Song, B.Q., Du, S.X., Gao, H.-J., 2011. Graphyne- and graphdiyne-based nanoribbons: density functional theory calculations of electronic structures. Appl. Phys. Lett. 98, 173102.
Pepper, M., Bursten, B.E., 1991. The electronic structure of actinide-containing molecules: a challenge to applied quantum chemistry. Chem. Rev. 91, 719–741.
Perdew, J.P., Burke, K., Ernzerhof, M., 1996. Generalized gradient approximation made simple. Phys. Rev. Lett. 77, 3865–3868.
Pye, C.C., Ziegler, T., 1999. An implementation of the conductor-like screening model of solvation within the Amsterdam density functional package. Theor. Chem. Acc. 101, 396–408.
Qu, N., Zhong, Y.-X., Schreckenbach, G., Pan, Q.-J., 2016. A computational investigation of polypyrrolic macrocyclic actinyl complexes: effects of explicit solvent coordination on structure, vibrational spectra and redox property. Theor. Chem. Acc. 135, 196.
Schmidt, A.-C., Nizovtsev, A.V., Scheurer, A., Heinemann, F.W., Meyer, K., 2012. Uranium-mediated reductive conversion of CO_2 to CO and carbonate in a single-vessel, closed synthetic cycle. Chem. Commun. 48, 8634–8636.
Schreckenbach, G., Shamov, G.A., 2010. Theoretical actinide molecular science. Acc. Chem. Res. 43, 19–29.
Schreckenbach, G., Hay, P.J., Martin, R.L., 1998. Theoretical study of stable trans and Cis Isomers in $[UO_2(OH)_4]^{2-}$ using relativistic density functional theory. Inorg. Chem. 37, 4442–4451.
Shao, L.-H., Biener, J., Jin, H.-J., Biener, M.M., Baumann, T.F., Weissmüller, J., 2012. Electrically tunable nanoporous carbon hybrid actuators. Adv. Func. Mat. 22, 3029–3034.
Sofer, Z., Jankovský, O., Šimek, P., Klímová, K., Macková, A., Pumera, M., 2014. Uranium- and thorium-doped graphene for efficient oxygen and hydrogen peroxide reduction. ACS Nano 8, 7106–7114.
Steele, H.M., Guillaumont, D., Moisy, P., 2013. Density functional theory calculations of the redox potentials of Actinide(VI)/Actinide (V) Couple in Water. J. Phys. Chem. A 117, 4500–4505.
Su, J., Chen, J., 2015. MOFs of Uranium and the Actinides. In: Cheng, P. (Ed.), Lanthanide Metal-Organic Frameworks. Springer Berlin Heidelberg, Berlin, Heidelberg, pp. 265–295.
Suwannakham, P., Chaiwongwattana, S., Sagarik, K., 2018. Mechanisms of photoexcitation and photoionization in small water clusters. RSC Adv. 8, 36731–36744.
Tang, Q., Zhou, Z., Chen, Z., 2013. Graphene-related nanomaterials: tuning properties by functionalization. Nanoscale 5, 4541–4583.
te Velde, G.T., Bickelhaupt, F.M., Baerends, E., Fonseca Guerra, C., Gisbergen, S., Snijders, J.G., Ziegler, T., 2001. Chem. ADF.
te Velde, G., Bickelhaupt, F.M., Baerends, E.J., Fonseca Guerra, C., van Gisbergen, S.J.A., Snijders, J.G., Ziegler, T., 2001. Chemistry with ADF. J. Comput. Chem. 22, 931–967.
Tian, G., Qi, Z., Ma, W., Wang, Y., 2017. On the catalytic activity of Pt supported by graphyne in the oxidation of ethanol. Chem. Select. 2, 2311–2321.
Vitova, T., Pidchenko, I., Fellhauer, D., Bagus, P.S., Joly, Y., Pruessmann, T., Bahl, S., Gonzalez-Robles, E., Rothe, J., Altmaier, M., Denecke, M.A., Geckeis, H., 2017. The role of the 5f valence orbitals of early actinides in chemical bonding. Nat. Commun. 8, 16053.
Walker, S.M., Halasyamani, P.S., Allen, S., O'Hare, D., 1999. From molecules to frameworks: variable dimensionality in the $UO_2(CH_3COO)_2·2H_2O$/HF(aq)/piperazine system. syntheses, structures, and characterization of zero-dimensional $(C_4N_2H_{12})UO_2F_4·3H_2O$, one-dimensional $(C_4N_2H_{12})_2U_2F_{12}·H_2O$, two-dimensional $(C_4N_2H_{12})_2(U_2O_4F_5)_4·11H_2O$, and three-dimensional $(C_4N_2H_{12})U_2O_4F_6$. J. Am. Chem. Soc. 121, 10513–10521.
Walsh, A.D., 1946. Ionisation potentials and bond order. Trans. Farad. Soc. 42, 779–789.
Wang, K.-X., Chen, J.-S., 2011. Extended structures and physicochemical properties of uranyl-organic compounds. Acc. Chem. Res. 44, 531–540.
Wang, S.S., Liu, H.B., Kan, X.N., Wang, L., Chen, Y.H., Su, B., Li, Y.L., Jiang, L., 2017. Superlyophilicity-facilitated synthesis reaction at the microscale: ordered graphdiyne stripe arrays. Small 13.
Wang, D., van Gunsteren, W.F., Chai, Z., 2012. Recent advances in computational actinoid chemistry. Chem. Soc. Rev. 41, 5836–5865.
Wu, G., Hu, Y., Zhao, J., Lan, T., Wang, D., Liu, Y., Chen, W., 2016. Ordered and active nanochannel electrode design for high-performance electrochemical actuator. Small 12, 4986–4992.
Xiao, K., Li, J., Wu, X., Liu, H., Huang, C., Li, Y., 2018. Nanoindentation of thin graphdiyne films: experiments and molecular dynamics simulation. Carbon.
Xue, Y., Huang, B., Yi, Y., Guo, Y., Zuo, Z., Li, Y., Jia, Z., Liu, H., Li, Y., 2018. Anchoring zero valence single atoms of nickel and iron on graphdiyne for hydrogen evolution. Nature. Commun. 9, 1460.
Yang, N., Liu, Y., Wen, H., Tang, Z., Zhao, H., Li, Y., Wang, D., 2013. Photocatalytic properties of graphdiyne and graphene modified TiO_2: from theory to experiment. ACS Nano 7, 1504–1512.
Yang, Z., Liu, R., Wang, N., He, J., Wang, K., Li, X., Shen, X., Wang, X., Lv, Q., Zhang, M., Luo, J., Jiu, T., Hou, Z., Huang, C., 2018. Triazine-graphdiyne: a new nitrogen-carbonous material and its application as an advanced rechargeable battery anode. Carbon 137, 442–450.
Yao, J., Wang, Y.-M., Pan, Q.-J., Guo, Y.-R., Zhang, H.-X., 2014. Structural/electronic properties and reaction energies of a series of mono- and bis-uranyl dihalides equatorially coordinated by N/O ligands. J. Mol. Model. 20, 2305.
Yao, J., Zheng, X.-J., Pan, Q.-J., Schreckenbach, G., 2015. Highly valence-diversified binuclear uranium complexes of a schiff-base polypyrrolic macrocycle: prediction of unusual structures, electronic properties, and formation reactions. Inorg. Chem. 54, 5438–5449.
Yin, X.-P., Wang, H.-J., Tang, S.-F., Lu, X.-L., Shu, M., Si, R., Lu, T.-B., 2018. Engineering the coordination environment of single-atom platinum anchored on graphdiyne for optimizing electrocatalytic hydrogen, evolution. Angew. Chem. Int. Ed. 57, 9382–9386.
Yuan, K., Ilton, E.S., Antonio, M.R., Li, Z., Cook, P.J., Becker, U., 2015. Electrochemical and spectroscopic evidence on the one-electron reduction of U(VI) to U(V) on magnetite. Environ. Sci. Technol. 49, 6206–6213.
Zhang, P., Ma, S., Sun, L.Z., 2016. Hydroxylated graphyne and graphdiyne: first-principles study. Appl. Surf. Sci. 361, 206–212.

Zhang, S., Wang, J., Li, Z., Zhao, R., Tong, L., Liu, Z., Zhang, J., Liu, Z., 2016. Raman spectra and corresponding strain effects in graphyne and graphdiyne. J. Phys. Chem. C 120, 10605–10613.

Zhao, H.-B., Zheng, M., Schreckenbach, G., Pan, Q.-J., 2017. Interfacial interaction of titania nanoparticles and ligated uranyl species: a relativistic DFT investigation. Inorg. Chem. 56, 2763–2776.

Zheng, Q., Luo, G., Liu, Q., Quhe, R., Zheng, J., Tang, K., Gao, Z., Nagase, S., Lu, J., 2012. Structural and electronic properties of bilayer and trilayer graphdiyne. Nanoscale 4, 3990–3996.

Zhong, Y.-X., Guo, Y.-R., Pan, Q.-J., 2016. A theoretical probe of high-valence uranium and transuranium silylamides: Structural and redox properties. Chem. Phys. Lett. 646, 75–80.

Zhou, J., Gao, X., Liu, R., Xie, Z., Yang, J., Zhang, S., Zhang, G., Liu, H., Li, Y., Zhang, J., Liu, Z., 2015. Synthesis of graphdiyne nanowalls using acetylenic coupling reaction. J. Am. Chem. Soc. 137, 7596–7599.

Zi, G., 2018. Recent developments in actinide metallacycles. Chem. Commun. 54, 7412–7430.